Modeling of recrystallization through the integration of disorientation and nucleation mechanisms: application to ferritic stainless steel

Louis Hennocque, Julie Favre, Nicolas Meyer, Thomas Sourisseau, Frank Montheillet, Laurence Latu-Romain, Guillaume Kermouche

Materials & Design 265 (2026) 115944

Contents lists available at ScienceDirect

Materials & Design

journal homepage: www.elsevier.com/locate/matdes

Modeling of recrystallization through the integration of disorientation and nucleation mechanisms: application to ferritic stainless steel

Louis Hennocque [a, b, c], Julie Favre [a,*], Nicolas Meyer [b], Thomas Sourisseau [b], Frank Montheillet [a], Laurence Latu-Romain [d], Guillaume Kermouche [a]

[a] Mines Saint-Etienne, Univ Lyon, CNRS, UMR 5307 LGF, Centre SMS, 158 cours Fauriel, 42023, Saint Etienne, France
[b] Centre de Recherches d'UGITECH, Ugine, 73400, France
[c] Safran Tech, Rue des Jeunes Bois, 78772, Magny-les-Hameaux, France
[d] Univ. Grenoble Alpes, CNRS, Grenoble INP, SIMaP, 38000, Grenoble, France

HIGHLIGHTS

- A unified framework captures continuous and discontinuous recrystallization in ferritic stainless steel.
- The model reproduces recrystallized fraction, nucleation frequency and grain-size trends at 900 °C.
- Subgrain misorientation build-up promotes nucleation through a thermodynamic criterion.
- Discontinuous nucleation dominates, while substructure evolution acts as a catalytic mechanism.

GRAPHICAL ABSTRACT

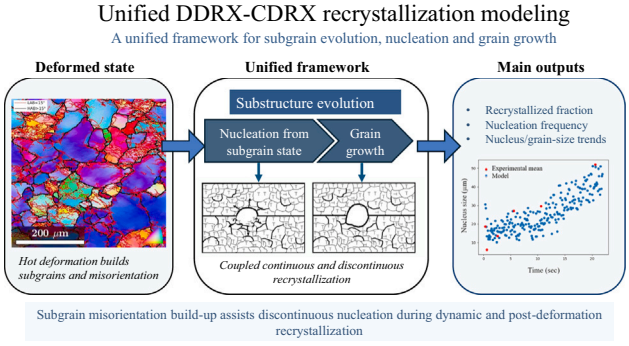

ARTICLE INFO

Keywords:
Characterization
Modeling/simulations
Iron alloys
Electron microscopy
Grains and interfaces

ABSTRACT

The mechanisms of continuous dynamic recrystallization (CDRX) and discontinuous dynamic recrystallization (DDRX) are usually treated as distinct in the literature. In this study, we propose a unified grain-scale framework that integrates both mechanisms. It combines subgrain boundary formation and misorientation, following the model originally proposed by Gourdet et al., and incorporates nucleation mechanisms through a thermodynamic formulation.

The framework was evaluated at 900 °C for a true strain of $\varepsilon = 0.6$ in a niobium-free ferritic stainless steel. Additional tests at $\varepsilon = 0.3$ and $\varepsilon = 0.6$ characterized the dynamic regime, followed by holding experiments to assess static evolution. Model predictions were validated against grain size distributions, recrystallized fractions, misorientation distributions, and the decay of subgrain boundary density.

Overall, the model demonstrates that CDRX and DDRX can be coupled within a simplified framework, providing a consistent description of both dynamic and static recrystallization regimes.

1. Introduction

Recrystallization is traditionally described as either a continuous or discontinuous process, each with its own formalismfor microstructure evolution during hot working [1–4]. The continuous mechanism accurately captures the dynamic regime in ferritic steels but offers limited insight into static phenomena, such as those observed during

* Corresponding author.
Email address: julie.favre@emse.fr (J. Favre).

https://doi.org/10.1016/j.matdes.2026.115944
Received 17 July 2025; Received in revised form 22 March 2026; Accepted 29 March 2026
Available online 3 April 2026

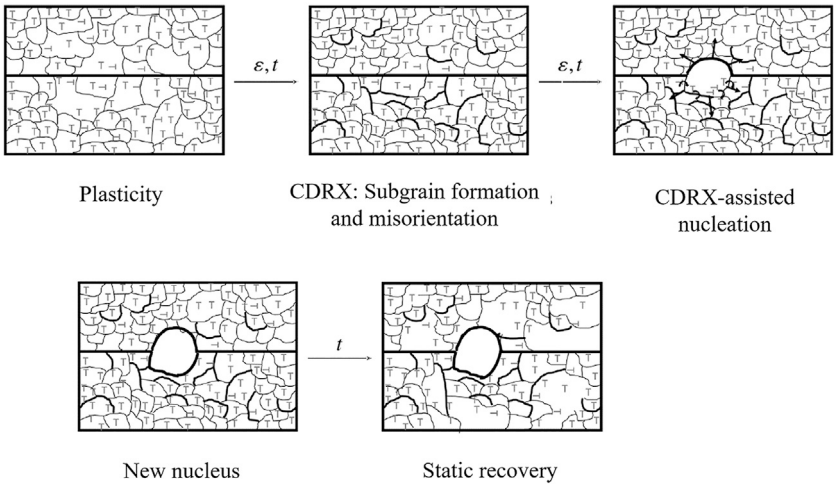

Fig. 1. Steps of the recrystallization process.

the post-deformation stage. In contrast, static nucleation is typically explained by bulging associated with discontinuous recrystallization. A unified framework for ferritic stainless steels therefore requires combining the two mechanisms within a single model. Such an approach would not only cover both regimes but also clarify intermediate cases where recrystallization involves a complex interplay of subgrain misorientation and boundary migration. Evidence increasingly suggests a continuum between DDRX and CDRX. Gardner and Grimes [5] identified a transition between these mechanisms in minerals, indicating that recrystallization may shift with deformation conditions. Derby [6] reported a power-law relation between grain size and flow stress, observed across materials regardless of mechanism, suggesting grain size is governed more by subgrain size than by the specific pathway. Thus, the distinction between continuous and discontinuous recrystallization appears gradual rather than absolute. Nucleation mechanisms also overlap. In discontinuous cases, serrations form and grow until nucleation occurs, while serration closure involves recovery phenomena similar to CDRX. For instance, magnesium alloys [7] show sub-boundary rotations induced by local shear, leading to DDRX at higher temperatures. In Al-Mg alloys [8], local plastic deformation and crystal rotation drive serration closure, again consistent with CDRX [9]. These examples highlight transitions influenced by temperature and purity [10], confirming that the boundary between DDRX and CDRX is often blurred, especially when strain gradients and stored energy vary within grains [11]. Mean-field modeling provides a practical tool [1,12,12–16], balancing predictive capability with modest computational cost compared to full-field approaches. From an industrial standpoint, it offers reliable results with relatively few parameters and extends beyond the limits of empirical models [6,17]. For high stacking fault energy materials such as ferritic stainless steels, mean-field models capture the gradual transformation of subgrain boundaries from low-angle (LAB) to high-angle (HAB) under deformation [18–24]. The reference model [1], initially developed for aluminum alloys, has since been refined and adapted to other materials through the inclusion of more complex mechanisms [19,20,22–24]. By contrast, DDRX models introduce nucleation through bulging (Strain-Induced Boundary Migration, SIBM) and are generally treated separately [12,25,26]. Static or post-dynamic recrystallization models describe grain size and recrystallized fraction over time, starting from a deformed state, but lack a consistent treatment of nucleation and subgrain misorientation. Such a description is essential to achieve a unified view of dynamic–static transitions [27,28]. Incorporating recent nucleation formulations would allow the model to include subgrain misorientation in predicting nucleation across both regimes [28,29]. Although nucleation is less frequent dynamically in high stacking fault energy materials, literature shows it remains possible. This study introduces a unified model that combines CDRX and DDRX mechanisms within a single framework, with three objectives (Fig. 1):

- **Integration of CDRX**: The model implements CDRX for each grain during the dynamic regime, with subgrain formation and misorientation governed by specific equations [1,2,30].
- **Incorporation of nucleation**: Nucleation is introduced through equations from recent work [31], enabling quantification and tracking of nucleation frequency.
- **Dynamic–static transition**: The model follows grain population evolution and quantifies recrystallized fractions within the microstructure.

This paper first details the experimental dataset for validation, then outlines the modeling steps and constitutive equations, implemented through an explicit finite difference scheme. Finally, predictions are compared with experiments, with emphasis on dynamic and static recrystallization regimes. This unified framework advances recrystallization modeling, delivering finer microstructural predictions and improved accuracy.

2. Material and methods

2.1. Material

The material, whose composition is detailed in Table 1, was a niobium-free ferritic stainless steel. It is close to conventional AISI 430, but with a higher Cr amount, slightly above 18 wt%, and low C and N contents so as to have a fully ferritic structure across the hot working temperature range. The grade was developed from elemental metals by Ugitech, France. The as-received material was smelted in a Vacuum Induction Melting (VIM) furnace and then cast into a 25 kg ingot. The latter was forged into bars of cross-section 18 mm x 38 mm. Finally, heat treatment of 40 minutes at 900 °C, followed by water quenching, was carried out on the bars to ensure a fully recrystallized state. The resulting microstructure had an initial grain size of 80 μm. Cylindrical samples, measuring 19.5 mm in height and 13 mm in diameter, were machined from the bars. The longitudinal axis of the specimen was aligned with the longitudinal axis of the bars.

2.2. Hot deformation

Uniaxial compression of these samples was carried out using a computer-controlled Schenck servo-hydraulic machine. To maintain a constant temperature in the test piece without any thermal gradients, an infrared heating furnace was employed. Two thermocouples inserted

Table 1
Composition of the studied ferritic stainless steel.

Type	C	Si	Mn	Ni	Cr	Mo	V	Cu	S	P	N	Nb	O (ppm)
Wt (%)	0.006	0.375	0.334	0.127	18.25	0.02	0.053	0.021	0.003	0.021	0.014	0.008	40

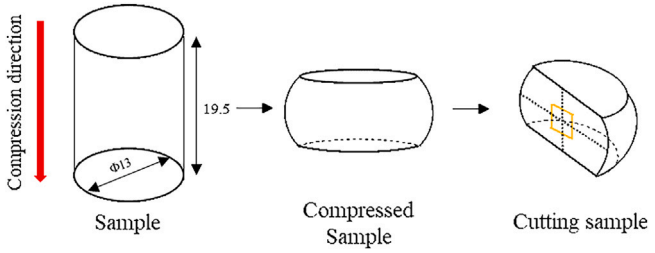

Fig. 2. Schematic diagram of the deformed sample after compression, showing the location of post-test sectioning.

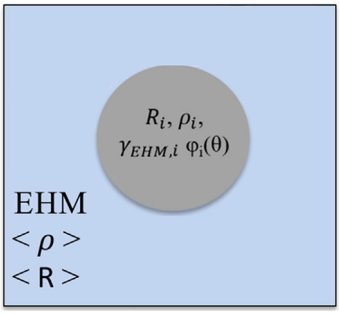

Fig. 3. Grain immersed in an average-type field environment.

into each compression anvil were used to control the sample temperature. Additionally, the system features a mechanical quenching system for rapid ejection and water quenching after deformation. To reduce friction during deformation, a graphite-based lubricant was used. A holding time of 10 minutes was applied before deformation to ensure a homogeneous temperature. Compression tests were carried out at a temperature of 900 °C with a true strain of 0.6, and a strain rate of 1 s^{-1}. Subsequently, a holding time of 2, 5, 10, and 20 s was applied before quenching the sample. The flow stress values were corrected to consider the effect of friction with the anvils. The correction was applied using a Tresca friction coefficient $\bar{m} = 0.05$ [32]. Adiabatic self-heating was estimated and taken into account for the different stress-strain curves. It is considered that 90% of the mechanical energy is retained in the compression specimen and contributes to the temperature increase [33].

2.3. Microstructure characterization

Cross-sections through the center of the compressed samples were prepared for characterization by EBSD. The samples were cut by Electrical Discharge Machining (EDM). Fig. 2 presents a schematic of the sample after the compression test, along with the subsequent sectioning location. A standard metallographic preparation was performed by mechanical polishing to a final grit of P4000 (5 µm SiC granulometry) followed by electropolishing with a 10% $HClO_4$ and 90% ethanol solution for 30 s at 32 V at room temperature. The microstructure observations were carried out on a Zeiss scanning electron microscope (SEM) equipped with a Field Emission Gun (FEG) tip, model Supra 55 VP. EBSD analysis was conducted with a Symmetry 2 camera with a CMOS detector from Oxford Instruments NanoAnalysis. EBSD data was collected using AztecHKL software. To balance the need for large statistical samples with the detailed characterization of substructure evolution, a trade-off was made by selecting a sufficiently small step size of 1 µm while conducting the analysis over a large area of 2.5 mm^2. Various possible camera modes allow for selecting the image size. For the presented characterizations, the second mode is used, which corresponds to an image size of 156×128 px^2. EBSD data were post-processed using MTEX, a free Matlab toolbox [34] for analyzing and modeling crystallographic textures using EBSD data. Minimum misorientation was taken at 1°, and lower values were disregarded. Below this threshold, the misorientation value is significantly affected by the measurement noise. A grain is defined as any closed contour of boundaries whose misorientation is greater than 15°. On the other hand, a subgrain is defined by boundaries with misorientation ranging from 1 to 15°, inclusive. The lowest size limit for detecting and taking into account subgrains is set at 10 pixels. The subgrain population is extracted from EBSD data using the `calcGrains` function of the MTEX toolbox with Matlab. The dataset is post-processed using Python's scikit-learn libraries [35].

3. Model structure

The model is inspired by the work of Cram et al. [12] within the dynamic regime. The polycrystalline structure of the material is represented by a set of spherical grains, each with its own unique attributes. Each grain is defined by its radius R, an individual Taylor factor M_i, and a dislocation density ρ_i. In the work presented here, the CDRX model is applied to each of the grains, allowing the generation of a substructure and the progressive misorientation of new sub-grains during deformation. A simple illustration showing grains represented in an average environment (Equivalent Homogeneous Medium, EHM) is presented in Fig. 3. The model is initialized by assigning fundamental parameters to each grain, which depend on temperature and strain rate. Specifically, the initialization process involves the random selection of properties such as grain size and Taylor factor M according to predefined distributions (see Table 2). This approach accounts, at least in part, for the potential effects of these distributed properties on the plasticity of the polycrystal, allowing for a gradual initiation of recrystallization over the entire grain population. The numerical time integration of the equations is performed using a finite difference scheme. It proceeds through successive time increments, each sufficiently small, and at each of these steps, various interdependent "blocks" are activated. A summary diagram (Fig. 4) introduces each of these blocks, which will be detailed later. The model includes:

- Input parameters for the model (grain size distribution, dislocation density ρ, hardening parameters h and r).
- Management of plasticity laws at each time or strain increment.
- Integration of the CDRX model, which evolves in each grain. The CDRX model derived from the work of Gourdet et al. [1,24] is used for this model.
- Management of nucleation with the criterion established in previous work [31].
- Grain growth based on Hillert's law [36], with integration of an additional pressure induced by the nucleation model approach.
- Transition between dynamic and static regimes, with time-based switching during holding periods.

Table 2
Table of parameters.

Variable name (units)	Value	Description
ϵ_{max}	0.6	Maximum strain
t_{max} (s)	22	Maximum time
initgrainsize (μm)	50	Initial grain size
$\langle M_T \rangle$	3.06	Average Taylor factor
σ_{M_T}	0.15	Standard deviation of Taylor factor
N_{grains}	500	Initial number of grains
α	0.3	Dislocation junction strength
T (K)	1173.15	Temperature
$\dot{\epsilon}_{\text{macro}}$ (s^{-1})	1	Macroscopic strain rate
b (m)	2.5×10^{-10}	Burgers vector
μ (Pa)	$10.8 \times 10^{10}\left(1 - 5.1 \times 10^{-4} T\right)$	Shear modulus
σ_e (Pa)	6.3×10^{7}	Yield stress
ρ_{ini} (m^{-2})	$\left(\frac{\sigma_e}{\langle M_T \rangle_{\text{ini}} \alpha \mu b}\right)^2$	Initial dislocation density
k (Pa $m^{1/2}$)	0.04	Hall-Petch constant in individual grains
γ (J m^{-2})	0.8	Grain boundary energy
t (s)	0	Time initialization
ϵ_{macro} (-)	0.0	Macroscopic strain
θ_0 (°)	1.0	Minimum misorientation
θ_C (°)	15.0	Maximum misorientation
$\Delta\theta_{\text{cl}}$ (°)	1	Class width in degrees
n	3	Number of slip systems
α_{gauss} (-)	0.3	Partitioning coefficient (CDRX)
τ (J)	$0.5 b^2 \mu$	Line energy (J)
h_0 (m^{-2})	3.7×10^{12}	Rheological parameter h_0
r_0 (m^{-1})	362	Rheological parameter r_0
m_r	0.0202	Exponent m_r
m_h	0.4893	Exponent m_h
Q_h (J mol^{-1})	103,341	Activation energy Q_h
Q_r (J mol^{-1})	1,962,613	Activation energy Q_r
Mob (m^2 s^{-1} J^{-1})	$3.5 \times 10^{-2} \exp\left(-\frac{254000}{8.31T}\right)$	Grain boundary mobility
Q_{SRX} (J mol^{-1})	200×10^{3}	Activation energy for static restoration
t_{SRX0} (s)	5×10^{-7}	Characteristic time for static restoration
K_{nuc}	4×10^{-5}	Amplitude for nucleation
n_{nuc}	3	Parameter for nucleation
grainsizelimit (m)	1×10^{-10}	Considered grain size limit
Hardened/recrystallized grain threshold (-)	100	/

3.1. Plasticity

Plasticity is integrated into the model through the Laasraoui-Jonas law, which applies to each grain with the relation:

$$\frac{d\rho}{d\epsilon} = h - r\rho \tag{1}$$

where h and r have been previously determined [24]. An iso-work hypothesis [37] is associated with the macroscopic deformation between the different grains, meaning that each grain undergoes the same work increment, according to the relation:

$$d\epsilon_i = \frac{K}{\sigma_i} \tag{2}$$

where K represents the macroscopic work increment across the studied volume, and σ_i represents the grain's current flow stress. This iso-work hypothesis implies that the hardest grains (in terms of orientation or hardening) deform the least. A Hall-Petch effect is included to account for the size effect on σ_i for each grain according to the equation:

$$\sigma_i = \sigma_0(\rho) + \frac{k}{\sqrt{d_i}} \tag{3}$$

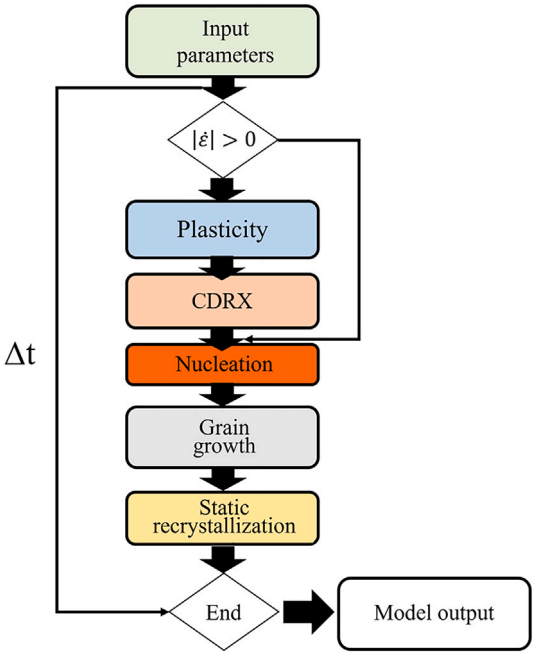

Fig. 4. Model structure inspired by the work of Cram and Hutchinson [12].

where k is a parameter (in this case, taken as 0.04 MPa.$m^{-1/2}$), and d_i is the size of grain i. The intrinsic value of the elastic limit σ_0 for a grain is given by the Taylor law, as recalled in Eq. (4).

$$\sigma_0 = M_i \alpha_T \mu b \sqrt{\rho_i} \tag{4}$$

where $\rho = \rho_0$ (see Table 2) initially, for a recrystallized state, ρ_i represents the dislocation density and M_i denotes the Taylor factor of the grain. Consequently, a grain with a higher flow stress is considered "harder," either due to hardening (with a high dislocation density ρ, leading to a high stress σ_0) or due to its small size. This results in a smaller strain increment according to Eq. (2). Conversely, a grain that is less hardened or larger in size will tend to undergo larger strain increments, which is physically consistent.

4. Grain-scale implementation of the CDRX model

The CDRX model is implemented at the grain level. The original formulation is adapted for consistency with other modules in the framework. For instance, the initial CDRX equations included substructure annihilation by boundary migration. This term is excluded here (see Eq. (6)) since grain growth already accounts for it in a separate module. The model relies on two main equations. The first estimates the progressive misorientation of existing sub-boundaries:

$$d\theta = \frac{b}{2n} \cdot (1 - \alpha_i) \cdot r \cdot \rho_i \cdot D_i \cdot d\varepsilon \tag{5}$$

where θ represents the misorientation of the created sub-boundaries, b is the Burgers vector (m), α_i is a partitioning coefficient, r is the parameter associated with dynamic recovery, ρ_i is the dislocation density in the grain (m^{-2}), n is the number of dislocation sets in the boundary, and D_i is the subgrain size (m). The second equation governs the creation rate of new sub-boundaries from the condensation of dislocations:

$$dS = dS_i^+ + \cancel{dS_i^-} = \frac{b}{n\theta_0} \alpha_i r d\varepsilon + \cancel{f_{HAB} S_i^2 v_{HAB} \frac{d\varepsilon}{\dot{\varepsilon}}} \tag{6}$$

The coefficient α_i modulates the relative weight of these two equations. Its value is distributed around 0.3, as determined in previous work [24], to reproduce the correct misorientation distribution.

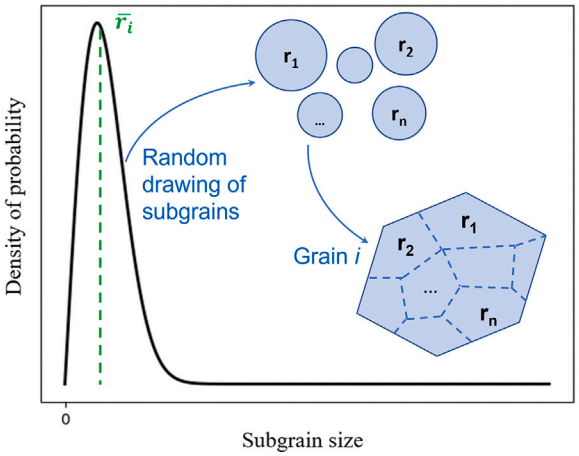

(a) Simulated distribution from a Rayleigh law centered on the mean subgrain size $\bar{r}_i$, derived from substructure density S_i.

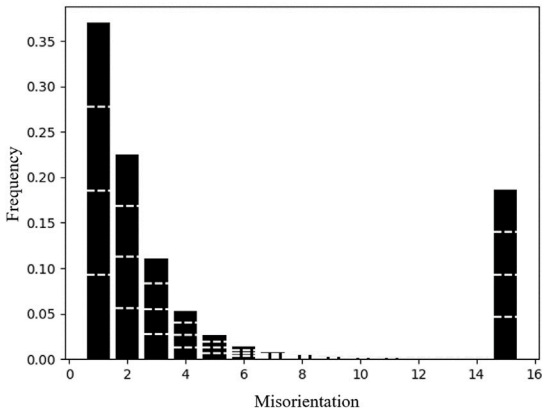

(b) Example misorientation distribution of a grain, fractioned into subgrain distributions.

Fig. 5. Subgrain size distribution and misorientation fractionation for population generation.

The objective of this CDRX calculation is to reproduce substructure density and misorientation distributions that match experimental data. This is achieved by adjusting α_i without introducing additional parameters.

At each time increment dt, the subgrain population is updated for every grain i with substructure density S_i. Initialization proceeds as follows: the average subgrain size $\bar{r}_i$ is obtained from S_i using the stereological relation $S_i = 3/2\bar{r}_i$. This mean size is then used as the center of a Rayleigh distribution, from which potential subgrain sizes are randomly sampled (Fig. 5(a)). The sampled set is iteratively adjusted until the total subgrain volume equals that of the parent grain and the average substructure density matches S_i. The sub-boundary area of each subgrain is estimated as:

$$S_{sg} = \frac{1}{2} \cdot 4\pi \cdot r_{sg}^2 \tag{7}$$

where the factor $\frac{1}{2}$ accounts for boundary sharing between neighboring subgrains. The sum of all S_{sg} divided by the grain volume must equal S_i; otherwise, the population is refined through iterations until convergence.

Misorientation distributions for individual subgrains are derived from the parent grain. The parent misorientation function is discretized, and random elements are assigned to subgrains (Fig. 5(b)). The last class, with $\theta \geq \theta_c = 15°$, represents high-angle grain boundaries (HABs) and is included, since some subgrains may intersect grain boundaries, raising their mean misorientation. In reality, subgrains adjacent to grain boundaries differ from those in the grain interior [24], but this distinction is not made here. Instead, all subgrains are given a non-zero probability of containing a boundary segment. In the recrystallized state, initialization is trivial since $S = 0$.

The final step is to estimate the surface energy γ_{sg} of each subgrain j in grain i, based on its misorientation θ_j. The Read–Shockley law is applied [38]:

$$\gamma_{sg} = \gamma \frac{\theta_j}{\theta_c} \left(1 - \ln\left(\frac{\theta_j}{\theta_c}\right)\right) \tag{8}$$

Together, these equations define the subgrain population and their surface energy distribution for each grain at any given time. During the static regime, CDRX equations are assumed inapplicable (Fig. 4). Substructure density then decays exponentially with time due to recovery, as described by the empirical relation 19. This decay increases the HAB/LAB ratio, which is accounted for by simple renormalization of the misorientation distribution. The distribution shape for $\theta < 15°$ is assumed unchanged, with amplitude decreasing, while the HAB class $\theta \geq 15°$ increases to represent the loss of substructure during recovery.

5. Nucleation

Reference [31] dedicated to the study of the nucleation phenomenon proposed a possible approach to describe nucleation processes by considering the specific contribution of the substructure. However, the implemented approach considered a subgrain interacting with an equivalent homogeneous medium (EHM), i.e., the entire polycrystal, for simplicity.

Within the proposed mean-field model, this description is refined to account for interactions within the subgrain population at a more local scale by considering an EHM for each grain. Consequently, the associated surface energies and the average subgrain size are specific to the evolution of each grain, providing a more accurate representation of the interactions between a subgrain and its immediate surroundings. For each grain, the model calculates the probability of nucleation associated with each subgrain within the grain. First, the critical nucleus radius for the i-th parent grain is computed as follows:

$$r_i^* = \frac{4\gamma}{2\tau\bar{\rho} + 2S_i\gamma_{\mathrm{int}_i} + \frac{4\gamma}{R_c}} \tag{9}$$

where γ is the grain boundary energy, τ is the dislocation line energy, γ_{int_i} is the average surface energy of the sub-boundaries calculated from Eq. (8) for the i-th grain, and R_c is the critical radius computed over the polycrystal and defined later in Eq. (15). Once r_i^* is known, the energy barrier ΔG_{tot} required for nucleation can be calculated according to [31]. The nucleation event probabilities p are calculated for each subgrain in the grain, and subsequently converted into a nucleation frequency:

$$f = K_{nuc}\left(\frac{p}{1-p}\right)^n, \text{ with } p = e^{-\frac{\Delta G_{tot}}{\Delta G_{sg}}} \tag{10}$$

where p is the probability that a subgrain will overcome the required energy barrier ΔG_{tot} for nucleation, ΔG_{sg} is its readily available internal energy, and f is the nucleation frequency expressed as a function of p and two empirical parameters, K_{nuc} and n. The detailed calculation of p and f is provided elsewhere [31].

Nucleation events are calculated for each subgrain, yielding a list of nucleation frequency values specific to each subgrain. The sum of these values represents the predicted number of nuclei formed within

a grain per unit of time. The nucleation frequency equation for a grain containing K subgrains is written as:

$$\dot{N}_{\text{grain}} = \sum_{k=1}^{K} K_{\text{nuc}} \left(\frac{p_k}{1 - p_k} \right)^n \tag{11}$$

where p_k corresponds to the list of probabilities for each subgrain k in the considered grain, and K_{nuc} and n are set to $K_{nuc} = 4 \times 10^{-5}$ and $n = 3$. This approach applies the nucleation equation locally at the grain level, resulting in the following relation (Eq. 12) for the nucleation frequency across the entire system, which consists of P grains:

$$\dot{N} = \sum_{j=1}^{P} \dot{N}_{\text{grain},j} \tag{12}$$

The number of nuclei that appear during the time step dt corresponds to the product of this time step and $\dot{N}$ calculated over the various modeled grains:

$$N = \dot{N} \times dt \tag{13}$$

This number of nuclei can be compared with experimental data to determine the appropriate parameter values, n and K_{nuc}, to use in Eq. (11). When the expected number of nuclei is below unity, a residual denoted N_{res} is accumulated and carried over to the next time step at $t + dt$. This approach enables the accumulation of nucleation potential over time, even when the conditions at a given time step do not immediately permit nucleation.

When a nucleation event occurs, the subgrain with the highest probability $p = p_{\max}$ is selected, as illustrated in Fig. 6. The size of the subgrain with $p_{\max}$ is then considered and compared with the value of the critical radius r_i^* calculated for the corresponding grain i. To ensure that the subgrain selected for nucleation can grow in a stable manner within the microstructure, the maximum of the two sizes is taken as the nucleus size:

$$r_{\text{nucleus}} = \max \left(r_{\text{sg}}(p_{\max}), r_i^* \right) \tag{14}$$

The volume V_{sg} of the corresponding subgrain is then subtracted from the parent grain's volume (Fig. 6). The properties of the newly created grain are randomly assigned using the initial parameters of the model. The Taylor factor and the parameter α_i are randomly drawn according to the same distributions used during model initialization. The new nucleus exhibits a substructure density of zero, as well as a dislocation density close to zero (set at $10^9\ \text{m}^{-2}$ to avoid numerical issues, which is the commonly considered threshold). This grain then follows the evolution of continuous dynamic recrystallization (CDRX) under dynamic or static regimes, along with associated growth, nucleation, and plasticity, during subsequent calculation increments (Fig. 4). For the parent grain, whose volume has been reduced, the assumption is made that nucleation does not affect either the misorientation of the sub-boundaries or the substructure density. The misorientation histogram, as well as the value of S of the parent grain, thus remains the same after the volume removal.

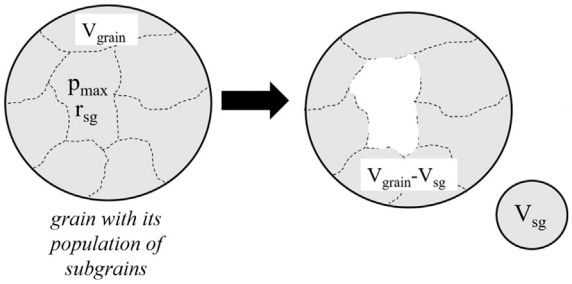

Fig. 6. Nucleation step: the subgrain with the highest probability p forms a new nucleus, and the parent-grain volume is updated accordingly.

6. Grain growth

The model incorporates grain growth based on Hillert's formulation [36], through two antagonistic terms in (1/R) that describe the growth of large grains at the expense of small grains under the influence of capillary forces. The critical radius R_c [39] is calculated for the entire polycrystal, in line with the mean-field assumption, to ensure volume conservation. The effect of dislocation density is also taken into account, again relative to an average value $\bar{\rho}$, weighted by the grain boundary areas to ensure volume conservation. A third term, ΔE_v, is introduced to account for the energy contribution of sub-boundaries, ensuring consistency with the various energetic terms used in the nucleation criterion, as described in [31]. The growth equation that gives the migration rate v_i is therefore:[1]

$$v_i = M\tau\left(\bar{\rho}(t) - \rho_i(t)\right) + 2M\gamma \left(\frac{1}{\bar{R}_c(t)} - \frac{1}{R(t)} \right) + M\,\Delta E_v \tag{15}$$

In particular, the third term, ΔE_v, which represents a volumic energy (J.m^{-3}), requires further explanation. This term reflects the stored energy associated with the internal sub-boundaries that are created. Therefore, it exists only for deformed grains, in which substructure density is present. Its formulation is entirely analogous to that of the dislocation density difference presented in the first term of Eq. (15). This term is thus expressed as the difference in stored volumetric energy within the sub-boundaries of a grain compared to the volumic energy of the equivalent homogeneous medium. Its expression is given by:

$$\Delta E_v = \overline{S_{\text{int}}(t) \cdot \gamma_{\text{int}}(t)} - S_{\text{int},i}(t)\,\gamma_{\text{int},i}(t) \tag{16}$$

The calculation of $S_{\text{int},i}(t)$ and $\gamma_{\text{int},i}(t)$ for each grain i derives from the CDRX model in each grain during deformation. This calculation proceeds by first estimating the substructure density and misorientation distribution, and then deducing the subgrain surface energy using the Read–Shockley law (Eq. 8).

By analogy with the other driving-pressure terms, the calculation of the average stored energy term at the polycrystal level is performed using an area-weighted average of grain boundary areas to ensure volume conservation. The relation can then be expressed as:

$$\overline{S_{\text{int}}(t) \cdot \gamma_{\text{int}}(t)} = \frac{\sum R_i^2 \cdot S_{\text{int},i}(t)\,\gamma_{\text{int},i}(t)}{\sum R_i^2} \tag{17}$$

At each time step, the migration velocity of each grain is therefore calculated based on Eq. (15). The grain size is updated using the following relation:

$$d_i = d_i + 2 \cdot v_i \cdot dt \tag{18}$$

where v_i represents the migration velocity of grain i. This migration velocity can be either positive or negative. In the case of a negative velocity, generally for the most heavily work-hardened grains, the associated size decreases, and the corresponding volumes are recalculated to

[1] The associated calculation for volume conservation is performed as follows:

$$\frac{dV}{dt} = 0, \quad V = \sum_i \frac{4\pi}{3} R_i^3$$

$$\frac{dV}{dt} = \frac{4\pi}{3} \cdot 3 \sum_i R_i^2 \frac{dR_i}{dt}$$

$$v_i = \frac{dR_i}{dt}, \quad v_i = M\left(\overline{\gamma_{\text{int},i} S_{\text{int},i}} - \gamma_{\text{int},i} S_{\text{int},i}\right)$$

$$\frac{dV}{dt} = 0 \Rightarrow \sum R_i^2 \left(\overline{\gamma_{\text{int},i} S_{\text{int},i}} - \gamma_{\text{int},i} S_{\text{int},i}\right) = 0$$

$$\Rightarrow \overline{\gamma_{\text{int},i} S_{\text{int},i}} = \frac{\sum R_i^2 \gamma_{\text{int},i} S_{\text{int},i}}{\sum R_i^2}$$

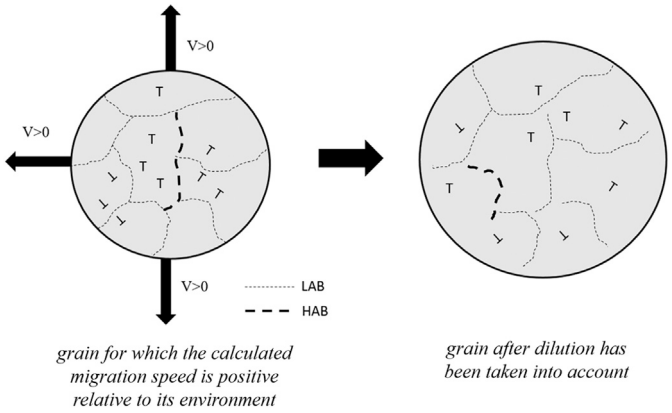

Fig. 7. Dilution effect imposed by a growing grain within the microstructure.

account for this change. The size can decrease to an arbitrary threshold value set at $d_i = 10^{-10}$ m to avoid numerical problems arising if grains have a zero or negative size. Below this size, grains disappear and are removed from the calculation.

When the migration velocity is positive, it results in an increase in the size of the corresponding grain in the model. In this case, several scenarios are taken into account, summarized in Fig. 7:

- If $v > 0$, a dilution effect is applied to the dislocation density within the grain. This dilution is given by the ratio of the old volume to the new volume, thereby accounting for the redistribution of dislocations within the grain.
- The same dilution effect is applied to the sub-boundary density S within the grain.
- Finally, it is assumed that when CDRX allows the formation of highly misoriented boundaries, the dilution effect applies only to these new grain boundaries created by plastic deformation, and not to the original grain boundaries that delimit the grain.

7. Calculation of the recrystallized fraction and nucleation frequency

The recrystallized fraction is typically defined as the volumetric fraction of material that has undergone recrystallization. However, a direct comparison between the calculated recrystallized fraction and the experimentally obtained one may lead to inconsistencies. Indeed, numerical and experimental definitions may differ:

- It is straightforward to compute from a model since all information is accessible and traceable numerically. From a numerical perspective, any grain that forms through recrystallization contributes to the recrystallized fraction. This could notably include grains that nucleated during the dynamic regime and then became work-hardened. Conversely, one might also observe deformed grains that were then recovered: these grains have never recrystallized in the strict sense but may have a very low level of work-hardening after static recovery.
- The experimentally determined recrystallized fraction usually follows a less strict definition: it refers to a fraction of the material with grains of significantly different morphology and low work-hardening. As observed in the analysis of microstructures, this fraction can, for example, be determined by thresholding GAM values on an EBSD map. However, this definition may accidentally include grains that were deformed and then strongly recovered, even if they did not recrystallize in the strict sense of nucleation.

To reconcile these two approaches and allow for comparison, it was decided to treat the modeled grain population as an experimental microstructure. Thus, both recrystallized fractions will follow the same definitions and be subject to the same biases, facilitating comparison. To this end, the recrystallized fraction at the end of modeling is defined as follows: a threshold is set in terms of substructure density; grains with low substructure density, and thus low work-hardening, are considered 'recrystallized', and their volume fraction constitutes the recrystallized fraction. Thus, grains that recrystallized early during the dynamic regime and then became heavily work-hardened will not be considered recrystallized. Similarly, grains that are very strongly recovered but not recrystallized by nucleation/growth will be considered recrystallized. This approach deliberately reproduces the two possible sources of bias present during experimental analysis, thereby allowing the comparison of quantities derived from a consistent definition.

The same comparison issue arises for counting the number of nuclei per unit volume. Although this quantity can be unambiguously defined numerically, experimental estimates are inevitably biased due to the 2D observation of a 3D polycrystal section. This bias is generally the weak point when comparing the nuclei population counted in 3D with that counted in 2D, as the experimentally observed surface typically contains far fewer nuclei than would be found in the total volume of the sample. To correct this bias, a method is proposed to simulate a metallographic section within a 3D modeled volume. A 2D area equal to the experimentally observed area (2.78 mm^2) is defined. This 2D area is then randomly populated by the different grains from the simulated population, without any specific preference, until the area is fully filled. The intersection between the cutting plane and each added grain is performed completely randomly. The number of nuclei and recovered grains on the 2D surface is then counted at different times during the simulation. By comparing the number of nuclei obtained with the experimental values, the nucleation frequency f of the model can be calibrated to ensure consistency between the simulation and experimental data.

A typical simulation of a section is shown in Fig. 8. The metallographic cut is represented by a height that depends on the average grain radius. Random grain positions are drawn along the z axis using a uniform law. In the example in Fig. 8, two grains are illustrated. The first, labeled R_1, is below the threshold and is considered part of the sample's volume but excluded from the calculation. However, the second grain, R_2, is intersected by the simulated "cut" of the sample and is therefore included in the nucleation frequency calculation. This simulation is repeated for all grains in the polycrystal over relevant time intervals.

8. Static recrystallization

Static recrystallization integrates quite naturally into the model. It is initially assumed that the mobility of grain boundaries does not change between the dynamic deformation regime and the static regime during which the grains are no longer deformed. Setting the deformation rate to zero involves several changes that have been discussed so far but are worth recalling in this context.

First, the CDRX equations are deactivated by construction when the deformation rate is set to zero. However, this does not mean that the

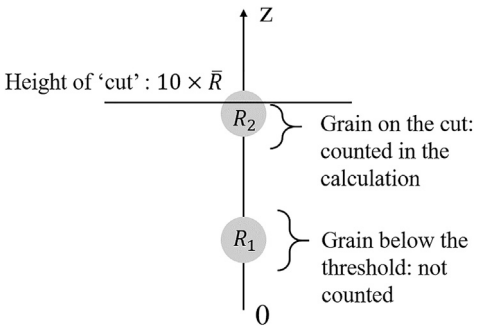

Fig. 8. Schematic representation of the simulated cut of a 2D analysis.

substructure no longer evolves; on the contrary, a decrease in the density of sub-boundaries is experimentally observed due to static recovery. An empirical law derived from the work of Jacquet et al. [18] describes the exponential decay of both the density of sub-boundaries and the density of free dislocations, according to the two equations applied during the static regime:

$$dS_i(t) = \frac{-S_i(t)}{t_{r_S}}\, dt, \tag{19}$$

where t_{r_S} is a characteristic time, considered as a fitting parameter initially, and:

$$d\rho_i(t) = \frac{-\rho_i(t)}{\tau_{RV}}\, dt \tag{20}$$

where τ_{RV} is also a characteristic time to be adjusted.

The misorientation distribution is updated to account for the disappearance of some sub-boundaries in the deformed regions for each characterized time. Thus, by construction, there is a growth of subgrains induced by the decrease in substructure density. From a statistical perspective, the increase in subgrain size induces an increase in the associated nucleation potential, counterbalanced by the decrease in the number of subgrains available for nucleation. It is the balance between these two antagonistic effects that ultimately predicts the evolution of the recrystallized fraction and nucleation frequency.

It should be noted that more mechanistic approaches are available in the literature to describe recovery, based for instance on dislocation-density evolution equations with explicit annihilation and rearrangement terms [40–42]. These frameworks, often coupled with recrystallization models [3,43], offer a physically-based alternative valid in both dynamic and static regimes. In this work, however, an empirical formulation was adopted to limit the number of state variables and parameters, while ensuring consistency with experimental observations.

9. Initial conditions and experimental validation

The initial grain size distribution is defined by a Rayleigh distribution centered on the experimental distribution. Typically, to account for 2D/3D discrepancies between experimental and simulated distributions, a factor of $\frac{\pi}{4}$ is often applied to account for the difference between the distributions [12]. However, it has been shown in the literature that the Rayleigh distribution (or a linear combination of such distributions) is the only invariant distribution in the transition (Abel transform) from the real 3D diameter distribution to the apparent 2D diameter distribution observed in a metallographic cross-section [44]. In this study, the distribution is therefore centered on the experimentally characterized distribution without using a correction factor. Henceforth, all distributions will be systematically represented in terms of area fraction.

A schematic representation of the simulation pathway is shown in Fig. 9. A deformation of 0.6 is applied at 1 s^{-1} followed by a holding time at 900 °C.

9.1. Key outputs of the recrystallization model

The model includes numerous elements that can be illustrated at any time or deformation level of the simulation. Among the key outputs are:

- The grain and subgrain size distributions
- The misorientation distribution within each grain, along with the associated subgrain boundary energy distributions
- The nucleation potential p to track the ability of the simulated microstructure to form new nuclei, as detailed in [31]
- The evolution of dislocation density and the resulting flow stress
- The substructure density per grain
- The recrystallized fraction

9.1.1. Evolution of subgrain distribution in dynamic and static regimes

Fig. 10 illustrates the typical evolution of a subgrain size distribution. The distributions plotted in blue correspond to the dynamic regime. As

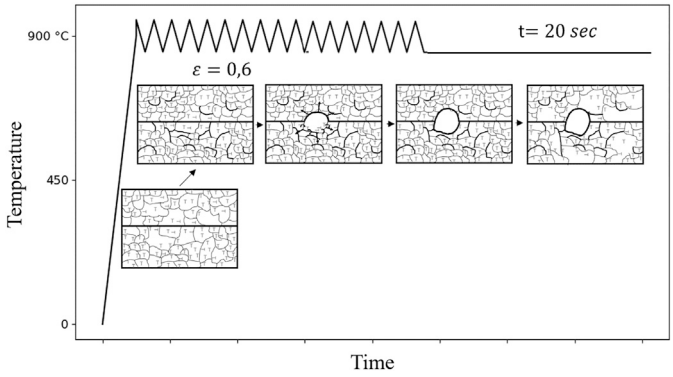

Fig. 9. Schematic representation of the simulation pathway. The expected evolutions described in the introduction are highlighted along the deformation path.

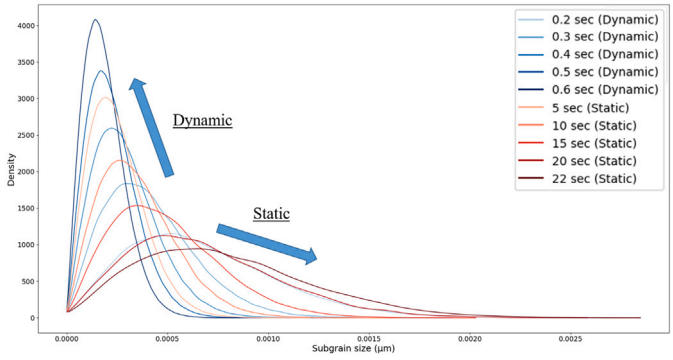

Fig. 10. Evolution of the simulated subgrain size distribution in dynamic (blue) and static (red) regimes (For interpretation of the references to colour in this figure legend, the reader is referred to the web version of this article.).

deformation increases, the size distribution narrows and shifts toward smaller values, indicating the progressive formation of smaller subgrains within a dense network of sub-boundaries. In red, the evolution of the subgrain size distribution with increasing time in the static regime can be observed. The substructure density follows an exponential decay, resulting in an increase in subgrain size, with a decreasing number of subgrains as the holding time progresses.

9.2. Comparison with experimental data: experimental validation

Various indicators are used to track and compare the model with experimental data. The CDRX module tracks the evolution of sub-boundary fractions relative to grain boundaries over time using misorientation distributions. The partitioning coefficient α, centered around 0.3, provides a good balance for accurately reproducing the evolution of the misorientation distribution and for yielding an appropriate substructure density. Fig. 11 illustrates the experimental (red) and simulated (black) distributions at the end of the deformation step. The simulation provides a good description of the experimental results, with minor deviations from the experimental data, indicating that the model accurately predicts the misorientation distribution during recrystallization.

9.2.1. Grain size distribution

The grain size distribution is a reliable indicator to visually assess the agreement between predicted and experimental microstructural evolution during deformation and holding. The experimental and modeled surface distributions are overlaid and tracked for different times during both regimes (Fig. 12). Certain grains, which exhibit biases due to metallographic sectioning, are excluded from the distribution. Specifically,

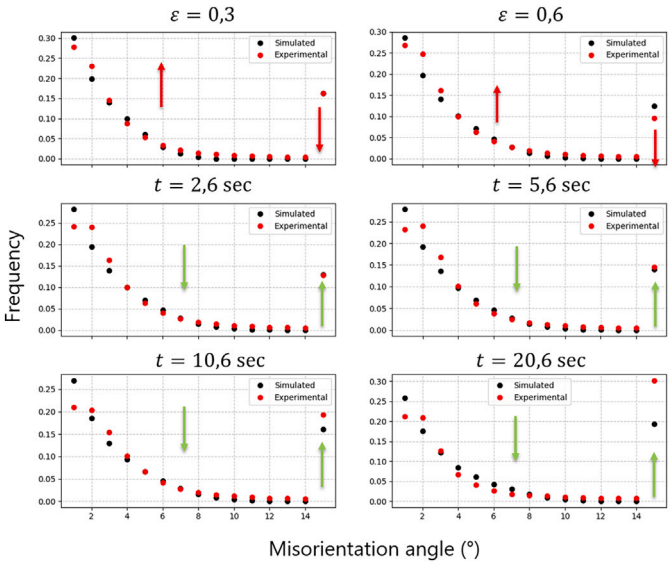

Fig. 11. Comparison of experimental (red) and simulated (black) misorientation distributions (For interpretation of the references to colour in this figure legend, the reader is referred to the web version of this article.).

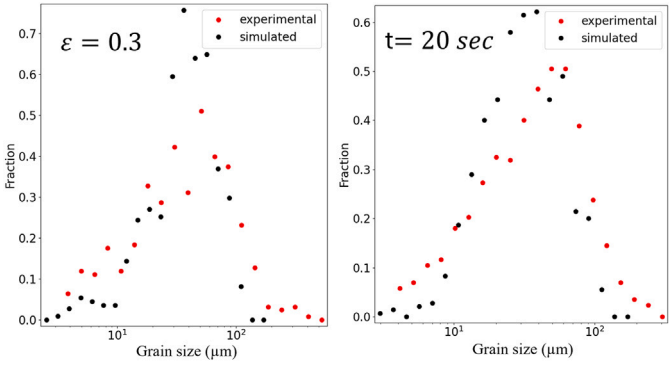

Fig. 12. Evolution of grain size distribution during deformation and holding.

grains located at the edge of the image are incomplete and thus excluded from the analysis. The model parameters are then adjusted to align the calculated distribution with the experimentally observed population.

The experimental distribution, shown in red, evolves relatively little during the dynamic and static regimes. One reason is that the kinetics of boundary migration are relatively slow at 900 °C. The distribution consists of a single mode, located between 20 and 100 µm for all studied times. This unimodal distribution may seem surprising, as a bimodal distribution is generally expected after recrystallization, where smaller grains typically correspond to recrystallized grains. The size of the recrystallized grains is likely very close to that of the parent grains.

9.2.2. *Tracking of nucleus size*

For each nucleation event predicted by the model, the emerging nucleus is tracked, and its size is plotted as a function of strain level or holding time in Fig. 13(a). The scatter plot (in blue) represents the nuclei predicted by the model, while the average size of recrystallized grains observed experimentally is shown in red. The model shows excellent agreement with experimental values, confirming the capability of the new nucleation formalism to predict realistic nucleus sizes.

During deformation, the nuclei predicted by the model and those observed experimentally tend to decrease in size. This results from the increase in substructure density predicted by the CDRX model. However, when deformation ceases, recovery phenomena induce a decrease in substructure density, leading to an increase in nucleus size, consistent with both the model's predictions and experimental characterizations. To facilitate the comparison between experimental data and the model, a second illustration is presented in Fig. 13(b). The scatter points representing the simulated nuclei in Fig. 13(a) have been smoothed to create Fig. 13(b). The resulting points, still in blue, are compared to the "box plots" representing the size distribution of recrystallized grains obtained from EBSD maps, with a GAM threshold set at 0.4°. This method provides a better visualization and comparison of the overall monotonic increase in modeled nucleus size over time during the static regime.

It is important to note that the dispersion of the experimental distribution (width of the box plot) increases with holding time. At 20 s, the extremes of the recrystallized grain distribution cover the entire range of grain sizes, from a few microns to over 100 microns. Nevertheless, the size of the modeled nuclei matches well with the averages of the experimental distributions, indicated by orange lines.

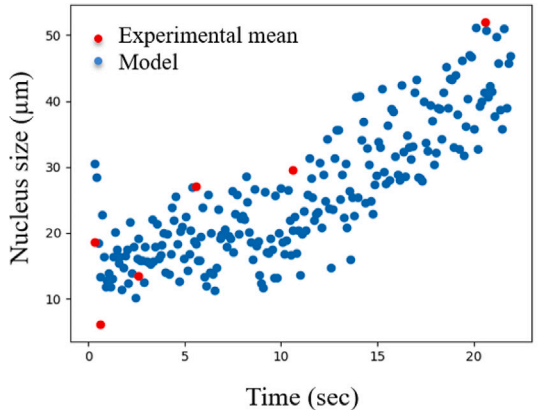

(a) Sizes of nuclei predicted by the model, shown as points (blue), compared to the average size of recrystallized grains (red)

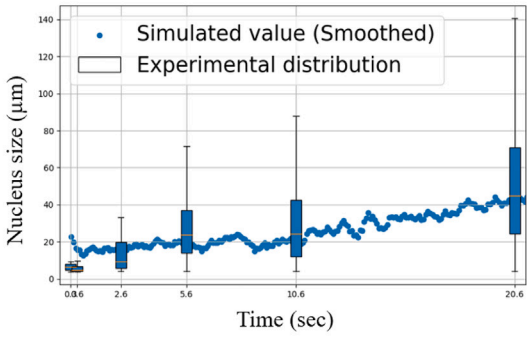

(b) Sizes of nuclei predicted by the model, numerically smoothed, shown as points (blue), compared with box plots representing the size distribution of recrystallized grains extracted at different times

Fig. 13. Comparison of predicted and observed sizes of nuclei and recrystallized grains.

However, the model slightly overestimates the size of the nuclei that appear during the dynamic regime, despite extensive parameter optimization. For deformations of 0.3 and 0.6, the average nucleus size is 20 and 15 microns, respectively. By contrast, experimental measurements show average sizes of around 10 microns, as indicated by the orange line on the box plot. This overestimation could be due to the assumption of homogeneous substructure construction during the dynamic regime, specific to the CDRX model, which likely overestimates the size of subgrains created, and therefore potential nuclei. A possible improvement for the model would be to account for the inhomogeneity of subgrain distribution within the grains. In particular, it would be beneficial to model the localization of subgrains at grain boundaries during the dynamic regime, potentially reducing the discrepancies predicted by the model.

For reference, experimental maps for different times are shown in Fig. 14. Recrystallized grains are identified based on an average misorientation angle below the threshold defined during post-processing (GAM < 0.4°). These grains, highlighted in blue, are extracted for each time in both the dynamic and static regimes (0.3; 0.6; 2.6; 5.6; 10.6; 20.6 s). As shown by the final map, at 20 s, the microstructure consists of nearly 60% of grains identified as recrystallized.

9.2.3. Recrystallized fraction and nucleation frequency

The maps presented in Fig. 14 are also used to compare nucleation frequency and recrystallized fraction. The recrystallized fraction provides information on the number and size of recrystallized grains. On the other hand, the nucleation frequency is used to compare the evolution of the number of nuclei per unit of time against experimental values. Unlike the nucleation frequency established in previous work [31], a 0.5-second hold time is applied after the dynamic phase (i.e., only for $t \geq 0.6$ seconds) in the modeling framework. This accounts for the delay before quenching that occurs experimentally. The nucleation frequency is thus calculated for the first point between $t = 0$ and $t = 1.1$ seconds.

Figs. 15(a) and (b) highlight the changes in the recrystallized fraction and the associated nucleation frequency. There is very good agreement for the increasing evolution of the recrystallized fraction. However, the model predicts a high recrystallized fraction at the initial state. This is an artifact: before deformation, the microstructure is relaxed and lightly work-hardened, making it appear as “recrystallized”. The model also provides an excellent description of the variations in nucleation frequency once the parameters are optimized. This confirms its ability to reproduce the trends observed experimentally. The nucleation frequency is initially very high at the end of the dynamic regime, then decreases

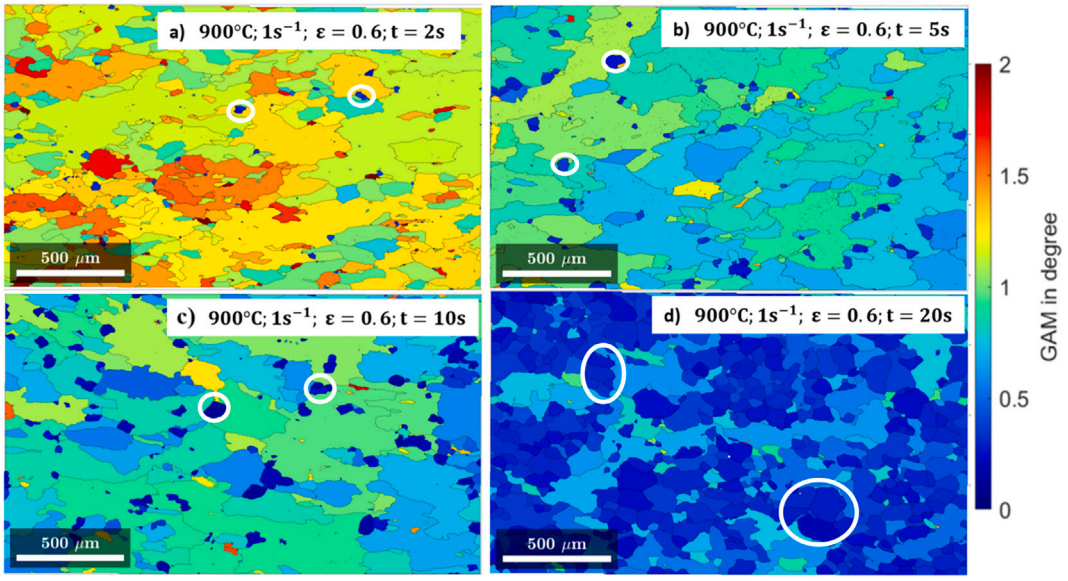

Fig. 14. GAM maps for different times after deformation at 900 °C; 1 s^{-1}; $\varepsilon = 0.6$: a) 2 sec after deformation, b) 5 sec after deformation, c) 10 sec after deformation, and d) 20 sec after deformation.

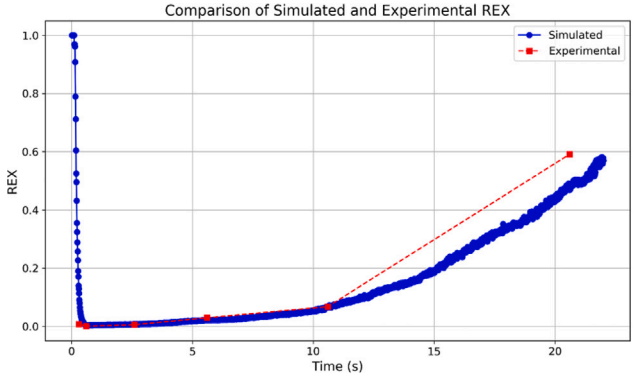

(a) Evolution of experimental and modeled recrystallized fraction

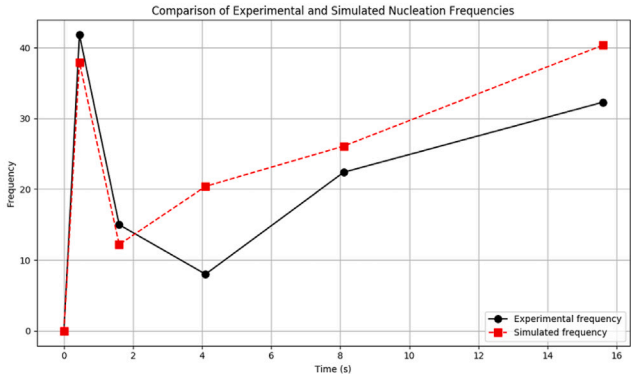

(b) Experimental and modeled nucleation frequency

Fig. 15. Comparison of experimental and modeled data.

rapidly during the static regime before showing a re-increase, primarily driven by static recovery effects.

9.3. Discussion

The integration of additional modules naturally leads to the addition of parameters compared to the previously mentioned models [1,2,12,30]. Parameters are listed and described below, whether they are experimentally justified or necessary for the proper functioning of the model. The setting of these parameters is often complex, and there is not always a readily available experimental procedure to determine them independently. This proliferation of parameters limits, to some extent, the applicability of the model to other case studies or its adaptation to different materials. The parameter choices made in this work are therefore explicitly documented, motivating each assumption and outlining the remaining limitations to guide future studies.

9.3.1. Parameters from the CDRX model

The substructure density is tracked experimentally and simulated using the CDRX model during dynamic conditions. Although experiments indicate that substructure density eventually saturates, the present implementation does not reproduce this effect. This saturation has been studied and explained in previous work on substructure heterogeneity [24]. Here, we deliberately omit this additional mechanism to avoid introducing further fitting parameters, as discussed in [24]. Despite this simplification, the model still matches the experimental data well, as seen in the first two points of Fig. 16.

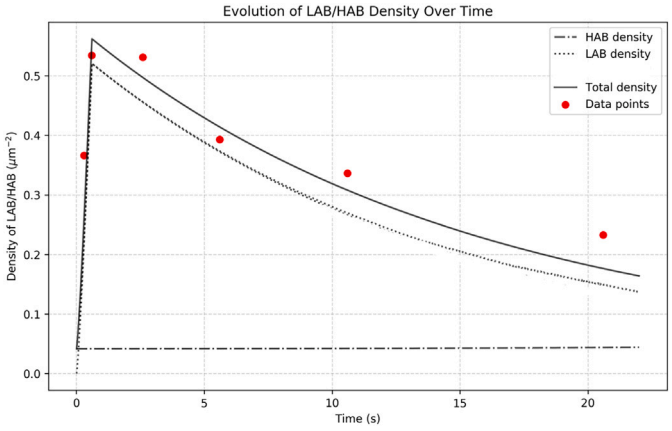

Fig. 16. Comparison of experimental and simulated substructure density.

Among the parameters of the CDRX model, n is set to 3, and the partitioning coefficient α is set to 0.3. The value of $n = 3$ is based on the order of magnitude used in the literature [18]. These two parameters, inherited from the original CDRX model, should be reconsidered and possibly reformulated in future studies to reduce model empiricism and improve transferability.

9.3.2. Adjustment parameters

This model contains two particularly sensitive parameters that merit further discussion. The first parameter relates to the decrease in substructure density t_{r_S} as a function of holding time in work-hardened zones. This parameter is adjusted for simulation purposes to reproduce the experimental results. This decay in substructure density cannot be predicted by the CDRX model, whose equations are adapted only for the dynamic regime. The physical phenomena associated with this parameter most likely correspond to subgrain coalescence and/or grain boundary migration effects.

The second highly sensitive parameter is the substructure threshold value used to distinguish between work-hardened and recrystallized grains. This threshold naturally influences the numerical outputs. Adjusting this value impacts the detection of nuclei in experimental data, thereby affecting the experimental values of $\dot{N}$. Consequently, it can influence the identification of other fitting parameters, such as the nucleation parameters in Eq. (11).

An example of output is shown by varying this parameter in Figs. 17(a) and (b) when this threshold changes. The result of this variation is the shift of the recrystallized fraction to a later time. Parameters such as experimental nucleation frequency values can also be affected by this threshold. This parameter is thus necessary in the current version of the model to ensure a precise fit to the experimental results. This threshold parameter is set once as a constant value because it is necessary for the construction of the model. Rather than being adjusted as a fitting parameter, it remains fixed throughout this work as a matter of convention. Assigning a firmer physical basis to this threshold would require an experimental separation between grains that truly recrystallized by nucleation/growth and grains that only recovered.

9.3.3. Parameters from nucleation

The parameters inherited from the nucleation criterion are K_{nuc} and n_{nuc} which determine the nucleation frequency from Eq. (11). In the case of the presented model, these parameters are calibrated to predict nucleation from subgrains. After optimization by a reverse method, the final values are $K_{\text{nuc}} = 4 \times 10^{-5}$ and $n_{\text{nuc}} = 3$.

Although a relative physical meaning can be assigned to these values and discussed in the corresponding work about nucleation [31], there remains a limit in the physical description of the proposed model. In

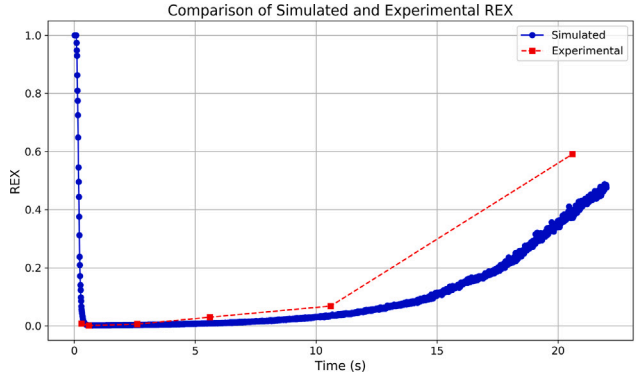

(a) Recrystallized fraction with a recrystallized/work-hardened threshold considered at 50 sub-grains/grain

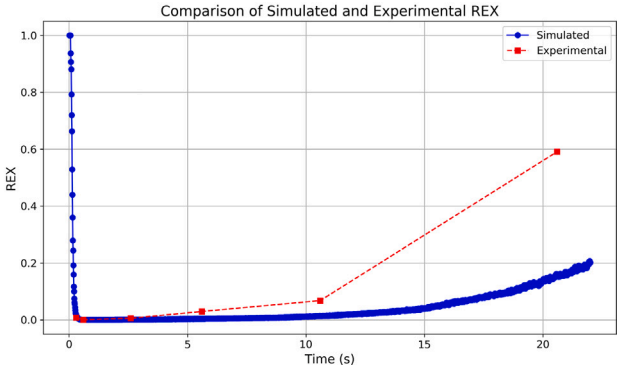

(b) Recrystallized fraction with a recrystallized/work-hardened threshold considered at 20 sub-grains/grain

Fig. 17. Comparison of recrystallized fractions at different GAM threshold values.

particular, K_{nuc} captures unresolved kinetics (e.g., site availability and interface mobility at the subgrain scale), and n_{nuc} tunes the nonlinearity of the probability–frequency mapping; both should be revisited as richer datasets become available.

10. Conclusions and perspectives

This work proposes a unified recrystallization model combining DDRX- and CDRX-type mechanisms within a grain-based framework. The model, calibrated on a ferritic stainless steel, accounts for both dynamic and static regimes through the description of subgrain populations and a substructure-driven nucleation criterion. Its ability to reproduce microstructural and substructural evolutions demonstrates the feasibility of coupling DDRX and CDRX within a single framework. The main innovativeness of this work lies in the unified integration of DDRX and CDRX mechanisms, providing a consistent description of recrystallization across regimes.

- A unified DDRX–CDRX model has been developed and applied to ferritic stainless steel, successfully reproducing recrystallized fraction, grain size, and misorientation distributions.
- A substructure-based nucleation criterion was introduced, providing a grain-scale description consistent with EBSD observations.
- The model highlights the interplay between subgrain formation, misorientation, and nucleation, offering insights beyond conventional approaches.
- Remaining limitations include the empirical description of static recovery and the use of a GAM threshold, which will require further refinement in future work.

Overall, the model establishes a step toward a more comprehensive description of recrystallization by bridging DDRX and CDRX mechanisms, while pointing to future perspectives such as mechanistic recovery equations and refined threshold criteria.

CRediT authorship contribution statement

Louis Hennocque: Writing – review & editing, Writing – original draft, Visualization, Validation, Supervision, Software, Project administration, Methodology, Formal analysis, Data curation, Conceptualization. **Julie Favre:** Writing – review & editing, Writing – original draft, Visualization, Validation, Supervision, Software, Resources, Project administration, Methodology, Investigation, Formal analysis, Conceptualization. **Nicolas Meyer:** Writing – review & editing, Writing – original draft, Visualization, Validation, Supervision, Software, Resources, Project administration, Methodology, Investigation, Funding acquisition, Formal analysis, Data curation, Conceptualization. **Thomas Sourisseau:** Supervision, Resources, Project administration, Investigation, Funding acquisition. **Frank Montheillet:** Writing – review & editing, Writing – original draft, Validation, Methodology, Conceptualization. **Laurence Latu-Romain:** Writing – review & editing, Writing – original draft, Visualization, Validation, Supervision, Software, Resources, Project administration, Methodology, Investigation, Funding acquisition. **Guillaume Kermouche:** Writing – review & editing, Writing – original draft, Visualization, Validation, Supervision, Resources, Project administration, Methodology, Investigation, Funding acquisition, Formal analysis, Conceptualization.

Declaration of competing interest

The authors declare that they have no known competing financial interests or personal relationships that could have appeared to influence the work reported in this paper.

Data availability

The authors do not have permission to share data.

References

[1] S. Gourdet, F. Montheillet, A model of continuous dynamic recrystallization, Acta Mater. 51 (9) (May 2003) 2685–2699.
[2] F.M.B. Ferraz, R.H. Buzolin, S. Ebenbauer, T. Leitner, A. Krumphals, M.C. Poletti, A predictive mesoscale model for continuous dynamic recrystallization, Int. J. Plast. 179 (Aug 2024) 104022.
[3] A. Rollett, F.J. Humphreys, G.S. Rohrer, M. Hatherly, Recrystallization and Related Annealing Phenomena, Elsevier, Feb 2004.
[4] T. Sakai, A. Belyakov, R. Kaibyshev, H. Miura, J.J. Jonas, Dynamic and post-dynamic recrystallization under hot, cold and severe plastic deformation conditions, Prog. Mater. Sci. 60 (Mar 2014) 130–207.
[5] K.J. Gardner, R. Grimes, Recrystallization during hot deformation of aluminium alloys, Met. Sci. 13 (3–4) (Mar 1979) 216–222.
[6] B. Derby, The dependence of grain size on stress during dynamic recrystallisation, Acta Metall. Mater. 39 (5) (May 1991) 955–962.
[7] A. Galiyev, R. Kaibyshev, G. Gottstein, Correlation of plastic deformation and dynamic recrystallization in magnesium alloy zk60, Acta Mater. 49 (7) (Apr 2001) 1199–1207.
[8] M.R. Drury, F.J. Humphreys, The development of microstructure in al-5mg during high temperature deformation, Acta Metall. 34 (11) (Nov 1986) 2259–2271.
[9] A.M. Wusatowska-Sarnek, H. Miura, T. Sakai, Nucleation and microtexture development under dynamic recrystallization of copper, Mater. Sci. Eng. A 323 (1) (Jan 2002) 177–186.
[10] K. Tanaka, M. Otsuka, H. Yamagata, Effect of orientation and purity on the dynamic recrystallization of aluminum single crystals with multi glide systems, Mater. Trans, JIM 40 (3) (1999) 242–247.
[11] K.A. Babu, Y.H. Mozumder, R. Saha, V.S. Sarma, S. Mandal, Hot-workability of super-304h exhibiting continuous to discontinuous dynamic recrystallization transition, Mater. Sci. Eng. A 734 (Sep 2018) 269–280.
[12] D.G. Cram, H.S. Zurob, Y.J.M. Brechet, C.R. Hutchinson, Modelling discontinuous dynamic recrystallization using a physically based model for nucleation, Acta Mater. 57 (17) (Oct 2009) 5218–5228.
[13] G. Smagghe, Modélisation de LA recristallisation lors du forgeage à chaud de l'acier 304l – une approche semi-topologique pour les modèles en champs moyens (Ph.D. thesis, HAL Id: tel-01665156v1), Mines Saint-Etienne, Feb 2017.
[14] K. Traka, E.S. Hernández, T. Nguyen-Minh, K. Sedighiani, J. Sietsma, L.A.I. Kestens, Prediction of different recrystallisation textures under a single unified physics-based model description, Acta Mater. 246 (2025) 113425.
[15] W. Wu, J. Park, W. Chen, G. Zhou, S.Y. Jo, P. Yang, C. Cui, W. Wang, M.-G. Lee, Integrated polycrystalline plasticity–cellular automaton model for microstructure evolution driven by discontinuous dynamic recrystallization during thermo-mechanical processing of magnesium alloys, Int. J. Plast. 193 (2025) 104437.
[16] B. Sułkowski, R. Chulist, Modeling of dynamic recrystallization texture in hot extruded MG, Comput. Mater. Sci. 201 (2023) 112968.
[17] J.J. Jonas, X. Quelennec, L. Jiang, E. Martin, The avrami kinetics of dynamic recrystallization, Acta Mater. 57 (9) (May 2009) 2748–2756.
[18] G. Jacquet, Etude De La Cinétique De Recristallisation Au Cours Du Laminage à Chaud D'aciers Inoxydables Ferritiques Stabilisés (Ph.D. thesis, HAL Id: tel-00975379), Mines Saint-Etienne, Oct 2013.
[19] R.H. Buzolin, M. Lasnik, A. Krumphals, M.C. Poletti, A dislocation-based model for the microstructure evolution and the flow stress of a ti5553 alloy, Int. J. Plast. 136 (Jan 2021) 102862.
[20] Y. Li, B. Gu, S. Jiang, Y. Liu, Z. Shi, J. Lin, A cdrx-based material model for hot deformation of aluminium alloys, Int. J. Plast. 134 (Nov 2020) 102844.
[21] M. Salojee, C.W. Siyasiya, K.A. Annan, J.S. Moema, Effects of strain and inter-pass time on the restoration behavior of 436 stainless steels, J. Mater. Eng. Perform. 34 (21) (2025) 25946–25953.
[22] Z.C. Sun, H.L. Wu, J. Cao, Z.K. Yin, Modeling of continuous dynamic recrystallization of al-zn-cu-mg alloy during hot deformation based on the internal-state-variable (ISV) method, Int. J. Plast. 106 (Jul 2018) 73–87.
[23] G. Maizza, R. Pero, M. Richetta, R. Montanari, Continuous dynamic recrystallization (cdrx) model for aluminum alloys, J. Mater. Sci. 53 (6) (Mar 2018) 4563–4573.
[24] L. Hennocque, J. Favre, N. Meyer, T. Sourisseau, D. Piot, L. Latu-Romain, G. Kermouche, Substructure heterogeneity during hot deformation of ferritic stainless steels - experimental characterization and discussion assisted by a mean-field model, Mater. Sci. Eng. A 906 (Jul 2024) 146335.
[25] J. Favre, D. Fabrègue, A. Chiba, Y. Bréchet, Nucleation of recrystallization in fine-grained materials: an extension of the bailey-hirsch criterion, Philos. Mag. Lett. 93 (Nov 2013).
[26] H.S. Zurob, Y. Bréchet, J. Dunlop, Quantitative criterion for recrystallization nucleation in single-phase alloys: prediction of critical strains and incubation times, Acta Mater. 54 (15) (Sep 2006) 3983–3990.
[27] M. Somani, S. Ghosh, J. Uusitalo, F. Hoffmann, M. Muratori, A. Smith, A.W. Abdelghany, Static recrystallization characteristics and kinetics of austenitic stainless steels under development for lh2 storage applications, Acta Mater. 259 (2025) 114750.
[28] P. Garcia-Chao, W. Kranendonk, C. Bos, J. Sietsma, S.E. Offerman, The mechanism of nucleation of static recrystallization in austenite after hot deformation, Acta Mater. 262 (2026) 115421.
[29] S. Liang, C. Liu, S. Guo, R. Li, S. Tao, S. Barella, A. Gruttadauria, M. Belfi, C. Mapelli, M. Abdelwahed, C. Yuan, Y. Peng, Construction of meta-dynamic recrystallization dynamic model of 316l stainless steel based on grain orientation spread during continuous variable rate thermal deformation, Metall. Mater. Trans. A 31 (2024) 3614–3628.

[30] F.M.B. Ferraz, R.H. Buzolin, M. Mabwohl, E. Shahryari, A. Krumphals, M.C. Poletti, A comprehensive mean-field approach to simulate the microstructure during the hot forming of ti-17, Mater. Sci. Eng. A 903 (2024) 146645.
[31] L. Hennocque, J. Favre, N. Meyer, T. Sourisseau, D. Piot, F. Montheillet, L. Latu-Romain, G. Kermouche, Nucleation of recrystallization: a new approach to consider the evolution of the substructure in the system, Materialia 38 (Dec 2024) 102301.
[32] F. Montheillet, Déformation à Chaud Des Métaux: Physique Et Mécanique, Ellipses, 2019.
[33] R.L. Goetz, S.L. Semiatin, The adiabatic correction factor for deformation heating during the uniaxial compression test, J. Mater. Eng. Perform. 10 (6) (Dec 2001) 710–717.
[34] R. Hielscher, H. Schaeben, et al., Mtex toolbox for texture analysis, 2022,. https://mtex-toolbox.github.io/ (Accessed: 22 Mar 2026).
[35] F. Pedregosa, G. Varoquaux, A. Gramfort, V. Michel, B. Thirion, O. Grisel, M. Blondel, P. Prettenhofer, R. Weiss, V. Dubourg, J. Vanderplas, A. Passos, D. Cournapeau, M. Brucher, M. Perrot, E. Duchesnay, Scikit-learn: machine learning in Python, J. Mach. Learn. Res. 12 (85) (2011) 2825–2830.
[36] M. Hillert, On the theory of normal and abnormal grain growth, Acta Metall. 13 (3) (1965) 227–238.
[37] O. Bouaziz, P. Buessler, Iso-work increment assumption for heterogeneous material behaviour modelling, Adv. Eng. Mater. 6 (1–2) (2004) 79–83.
[38] W.T. Read, W. Shockley, Dislocation models of crystal grain boundaries, Phys. Rev. 78 (3) (May 1950) 275–289.
[39] O. Beltran, K. Huang, R.E. Logé, A mean field model of dynamic and post-dynamic recrystallization predicting kinetics, grain size and flow stress, Comput. Mater. Sci. 102 (May 2015) 293–303.
[40] U.F. Kocks, H. Mecking, Physics and phenomenology of strain hardening: the fcc case, Acta Mater. 48 (3) (2003) 171–273.
[41] E. Nes, Modelling of work hardening and stress saturation in fcc metals, Prog. Mater. Sci. 41 (3) (1997) 129–193.
[42] Y. Estrin, Dislocation-density–related constitutive modeling, In A.S. Krausz, K. Krausz (Eds.), Unified Constitutive Laws of Plastic Deformation, chapter 2, Elsevier, 1996, pp. 69–106.
[43] K. Huang, R. Logé, A review of dynamic recrystallization phenomena in metallic materials, Mater. Des. 111 (2016) 548–574.
[44] S.D. Wicksell, The corpuscle problem: a mathematical study of a biometric problem, Biometrika 17 (1/2) (1925) 84–99.